Performance characterisation and printing parameter modelling of selective laser melting printed capillary wicks

Xu Meng
Changchun Institute of Optics, Fine Mechanics and Physics, Chinese Academy of Science, Changchun, China and Centre of Materials Science and Optoelectronic Engineering, University of Chinese Academy of Science, Beijing, China

Shujie Tan and Liping Ding
College of Mechanical and Electrical Engineering, Nanjing University of Aeronautics and Astronautics, Nanjing, China

Yicha Zhang
ICB-COMM, UMR 6303, CNRS, University Bourgogne Franche-Comté, UTBM, Belfort, France and Department of Mechanical Engineering and Design (Génie Mécanique et Conception), Universite de Technologie de Belfort-Montbeliard – Campus de Sevenans, Sevenans, France, and

Liheng Chen
Academy of Science, Changchun, China and Centre of Materials Science and Optoelectronic Engineering, University of Chinese Academy of Science, Beijing, China

Abstract

Purpose – The objective of this study is to investigate the feasibility of using selective laser melting (SLM) process to print fine capillary wick porous structures for heat pipe applications and clarify the interrelations between the printing parameters and the structure functional performance to form guidelines for design and printing preparation.

Design/methodology/approach – A new toolpath-based construction method is adopted to prepare the printing of capillary wick with fine pores in SLM process. This method uses physical melting toolpath profile with associated printing parameters to directly define slices and assemble them into a printing data model to ensure manufacturability and reduce precision loss of data model transformation in the printing preparation stage. The performance of the sample was characterised by a set of standard experiments and the relationship between the printing parameters and the structure performance is modeled.

Findings – The results show that SLM-printed capillary wick porous structures exhibit better performance in terms of pore diameter and related permeability than that of structures formed using traditional sintering methods, generally 15 times greater. The print hatching space and infilling pattern have a critical impact on functional porosity and permeability. An empirical formula was obtained to describe this impact and can serve as a reference for the design and printing of capillary wicks in future applications.

Originality/value – This research proves the feasibility of using SLM process to printing functional capillary wicks in extremely fine pores with improved functional performance. It is the first time to reveal the relations among the pore shapes, printing parameters and functional performance. The research results can be used as a reference for heat pipe design and printing in future industrial applications.

Keywords Additive manufacturing, Capillary wick, Heat pipe, Permeability

Paper type Research paper

Parameter description TI150 3D printing parameters

Laser scanning speed	=	6 m/s;
Laser scanning power	=	75 W;
Laser spot diameter	=	40 μm;
Powder spreading thickness	=	50 μm;
Laser hatch space	=	0.18–0.3 mm; and
Molding space	=	250 × 250 × 325 mm.

The current issue and full text archive of this journal is available on Emerald Insight at: **https://www.emerald.com/insight/1355-2546.htm**

Rapid Prototyping Journal
28/8 (2022) 1558–1572

[ISSN 1355-2546]
[DOI 10.1108/RPJ-06-2021-0127]

Nomenclature

A	=	Area (m^2);
R	=	Pore size (μm);
ε	=	Functional porosity (%);
K	=	Permeability (m^2);
h	=	Laser hatch space (mm);
M	=	Quality (kg);
ρ	=	Density (kg/cm^3);

This research was supported by the Fengyun-3 satellite project funding and the technical support was provided by the Nanjing Profeta Intelligent Technology Co Ltd.

Received 3 June 2021
Revised 16 January 2022
Accepted 23 February 2022

L = Working fluid;
ΔP= Pressure drops (Pa); and
v = Velocity of the liquid (m/s).

Capillary wick test piece size

Wick width (mm) = 20;
Wick length (mm) = 20; and
Wick height (mm) = 1.

Physical parameters of working fluid

Density, ρ = 1,000 kg/m^3;
Surface tension, σ = 70 N/m;
Viscosity, μ = 2.98×10^{-3} Pa s; and
Latent heat of vapourisation, h_{fv}= 2,260 kJ/kg.

1. Introduction

With the rapid development of aerospace technology, the functions of satellites have become increasingly diversified, leading to an increase in payloads and heat power. Heat dissipation problems can occur, such as heat accumulation in the narrow space of the satellite load and uneven temperature distribution in parts (Escobar *et al.*, 2016), increasing the thermal conductivity requirements for heat dissipation components to maintain thermal control. A heat pipe is a heat transfer device that uses the evaporation–condenser cycle of the working fluid to transfer heat from one location to another. It achieves high thermal conductivity through phase change for heat conduction (Sözen *et al.*, 2019). Heat pipes have been widely used in spacecraft thermal control technology for their high thermal conductivity, temperature uniformity and compactness (Bonnici *et al.*, 2019). The capillary wick is the wick structure of the heat pipe; it provides a return channel and power for the working fluid in the heat pipe (Shittu *et al.*, 2020). Traditional capillary wicks in heat pipes include (Faghri, 1995) grooved wicks formed by cutting, wire mesh-sintered wicks obtained by superimposed wire mesh sintering and powder-sintered wicks obtained by loose-powder sintering. A groove wick formed by the traditional cutting process has a high permeability, but its capillary suction force is small and the processing cost is high (Wong and Liao, 2018). The adaptability of the superimposed screen sintering process is too poor for mass production (Yan *et al.*, 2020). Although the permeability of a powder-sintered wick is small, the shape and size of each part of the capillary wick cannot be controlled. In addition, special-shaped heat pipes are difficult to manufacture because they have low structural strength (Faghri, 2012). Traditional methods have limitations in the manufacturing of high-performance heat pipe wicks; it is difficult to manufacture special-shaped heat pipes and internal integrated heat pipe parts.

In recent years, metallic additive manufacturing (AM) technology has matured and the precise printing of metal microstructures has been realised (Lebaal *et al.*, 2019; Zhang *et al.*, 2020; Lu *et al.*, 2020). Metallic AM technology can be a solution for the manufacturing of high-performance fine-capillary wick porous structures for heat pipes, without the complex processes and high costs of traditional heat pipe manufacturing methods. Moreover, 3D printing allows free forming, especially for printing internal channels (Vaneker *et al.*, 2020). Thus, it is possible to print capillary wicks with irregular shapes for heat pipes to be integrated into component structures to meet the heat conduction and weight requirements of the satellite components. Several researchers have recognised the prospects of 3D printing in the manufacture of heat pipe capillary wick structures, including the lightweight component design and part consolidation design for space engineering.

Jafari *et al.* (2017) designed and printed a frame-type porous capillary wick structure with 316 stainless steel and experimentally tested the functional porosity, capillary rise height and thermal conductivity of the printed capillary wick with different liquid working media. Their studies showed that the selective laser melting (SLM) technology can be used to print loop heat pipe (LHP) capillary wicks. For different working fluids, the effective thermal conductivity is 1.8–6.0 W/m K. Jafari *et al.* (2018) experimentally tested a porous capillary wick structure with a pore diameter of 216 μm printed by SLM. They found that the printed capillary wick cloud enhanced the heat transfer performance of the heat pipe with an increase in the capillary size according to $h(t)$–$t^{(1/3)}$ in the intermediate stage, although gravity affected the rise of liquid in the capillary wick. Esarte *et al.* (2019) designed and 3D-printed a frame-type 316 stainless steel capillary wick porous structure for an LHP with a heat transfer requirement of 80 W and experimentally tested its permeability and capillary rise height. The results showed that the permeability of an SLM capillary wick is two orders of magnitude greater than that of a powder-sintered capillary wick. Hu *et al.* (2020) 3D-printed an LHP capillary wick and studied the effect of the pore diameter (R) on the heat transfer performance. The results showed that the stainless steel LHP with a 3D-printed capillary wick (R = 200 μm) can be successfully started in approximately 100 s under a low thermal load of 20 W (2.83 W/cm^2). When the evaporator wall temperature is 100°C, the LHP can operate stably in a thermal load range of 20–160 W.

Figure 1 summarises the previous studies on 3D printing of capillary wicks; all of them used the SLM process and the samples were printed on 316 stainless steel. However, there is a lack of research on printing with other metallic materials. In addition, the previous capillary wick models were all frame structures with straight quadrilateral pores and a manufactured capillary wick with a single pore diameter. No research has been conducted on the influence of the capillary wick hole shape on the 3D capillary wick formation and permeability. Further, the relationship between the manufacturing parameters and the capillary wick performance parameters has not been explored.

The previous studies were the preliminary studies in this area; they mostly focused on the feasibility of 3D-printed capillary wicks. There was no deep analysis of their performance with different pore shapes. Furthermore, there has been no research on the relationship between 3 D-printing manufacturing parameters and capillary wick performance, which is critical in actual applications. Thus, this study conducts performance characterisation and printing parameter modelling of SLM-printed capillary wicks. Two types of capillary wick structures with different pore shapes were

Figure 1 Existing 3D capillary wick manufacturing method

Author, Years	Machine and Material	Method	Structure model
Davoud Jafari, Wessel W. Wits etc. (2017)	Concept Laser Mlab Cusing 90 stainless steel 316L	SLM	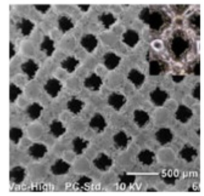
Davoud Jafaria, Wessel W etc. Wits (2018)	Concept Laser Mlab Cusing 90 stainless steel 316L	SLM	
Jesús Esarte, Jesús M. Blanco etc. (2019)	Copper powder	SLM	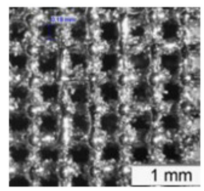
Zhuohuan Hua, Dongcheng Wang etc. (2020)	HBD100 stainless steel 316L	SLM	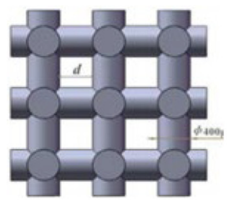

designed and a series of capillary wick test pieces with different pore diameters were generated by controlling the printing parameters and hatch space (h) for performance benchmarking. Based on the collected experimental datasets, an empirical model was built to describe the implicit relationships between the processing parameters, laser hatching space and performance of the printed capillary wick test pieces. The results of this research can be used as a reference for capillary wick design and printing in industrial applications.

The remainder of this paper is organised as follows: Section 2 introduces the sample preparation details; Section 3 presents the characterisation methods, devices and process; Section 4 presents the experimental results, modelling details and discussion; and Section 5 presents the conclusions and perspectives on future work.

2. Capillary wick sample preparation

2.1 Layer tool path construction structure

In SLM process, the manufacturability of porous structure or lattice structure is hard to check (Vaneker *et al.*, 2020; Lebaal *et al.*, 2019). Printing failure is often and especially for structures with fine pores, e.g. less than 300 μm. To print capillary wick with acceptable accuracy and achieve parametric control for experiment in this research, a new toolpath-based construction method, proposed in Zhang *et al.* (2021), is adopted to prepare the sample printing. This method uses physical melting toolpath profile with associated printing parameters to directly define slices and then assembly the generated slices into a processing/printing model. It can avoid the accuracy loss in the meshing, slicing and toolpath generation stages as that of traditional printing preparation methods. In addition, the manufacturability can be ensured because the slices are defined by deposition/melting profiles. As shown in Figure 2, the path-defined porous structure is spliced by the melt tracks. Therefore, the manufacturability and pore size of the porous structure are determined by the melt tracks. Therefore, path-planning parameters such as laser power, scanning speed, hatch space and layer thickness will affect the melt track's formation and its size.

As shown in the example in Figure 3, the hatch space of the quadrilateral and hexagonal line-filled cells is defined as the distance between two parallel paths.

2.2 3D printing of capillary wick

The SLM process was used to manufacture the test pieces. To investigate the influence of pore shape on the performance of 3D-printed capillary wick test pieces and the effect of

Figure 2 Illustrative examples of porous structures defined by printing paths: (a) quadrilateral pore and (b) hexagonal pore

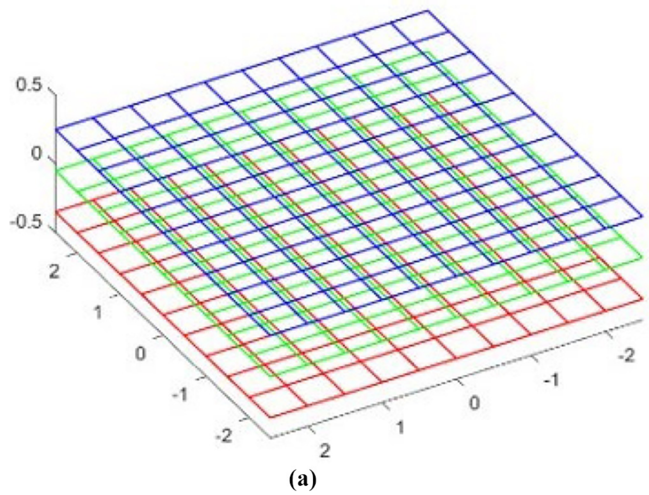

Figure 3 Schematic diagram of path-defined porous structures with different pore shape: (a) quadrilateral pore and (b) hexagonal pore

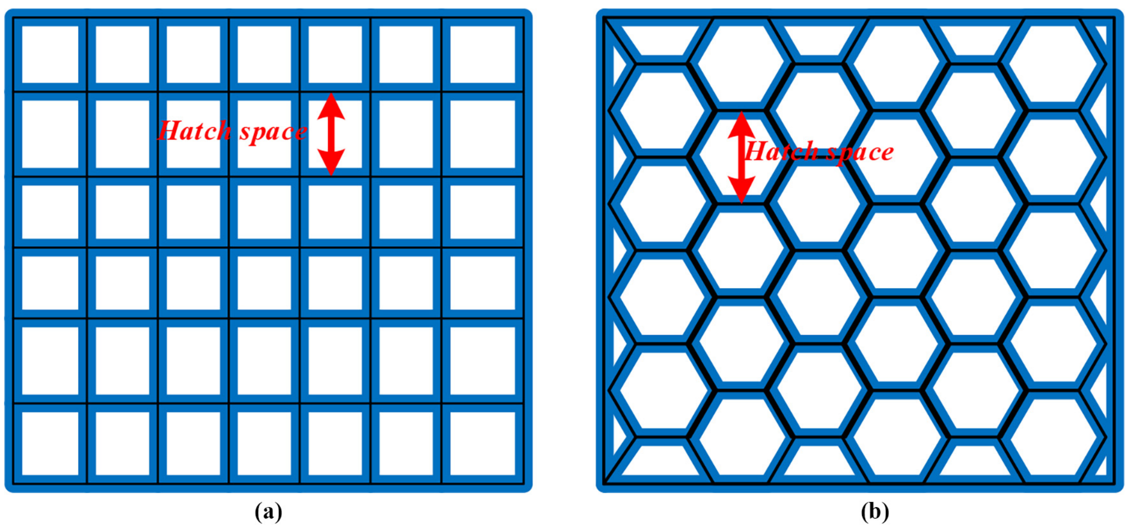

processing parameters on the porous structure printing result, 18 capillary wick test pieces with two shapes were printed using different laser scanning hatch space values.

To consider aerospace applications, titanium alloy (Ti6Al4V powder) was used for printing the capillary wick samples, as most mechanical structures in space are made of titanium alloy. A commercial printer (Ti150 3D printer) was used for printing. Figure 4 shows the material and printing device. Each sample had a length and width of 25 mm and a thickness of 1 mm. The scanning path and the laser hatch space (0.14–0.30 mm) differed among the samples. By changing these parameters, the metal powders were melted to form porous structures with internal channels used for liquid flow. The general sample manufacturing process included three main steps: pre-processing, printing and post-processing. The details are presented in Figure 5.

2.2.1 Pre-processing
The processing trajectory was generated in a homemade trajectory planning script. The cross-sectional diagram and trajectory planning diagram of the two types of capillary wicks are shown in Figures 4 and 5, respectively. The trajectory parameters are presented in Table 1.

2.2.2 Printing
The sample was printed with Ti150 equipment (Profeta, China) using Ti6Al4V powder (Zhonghang Maite, China). The printing parameters are presented in Table 2.

2.2.3 Post-processing
After printing, the samples were annealed using a heat treatment furnace as follows: the sample was maintained at 820°C for 2 h and cooled in the furnace to eliminate residual stress; after heat treatment, wire cutting was used to cut the

Rapid Prototyping Journal
Volume 28 · Number 8 · 2022 · 1558–1572

Figure 4 (a) Ti150 machine; (b) scanning electron microscope image of Ti6Al4V powder

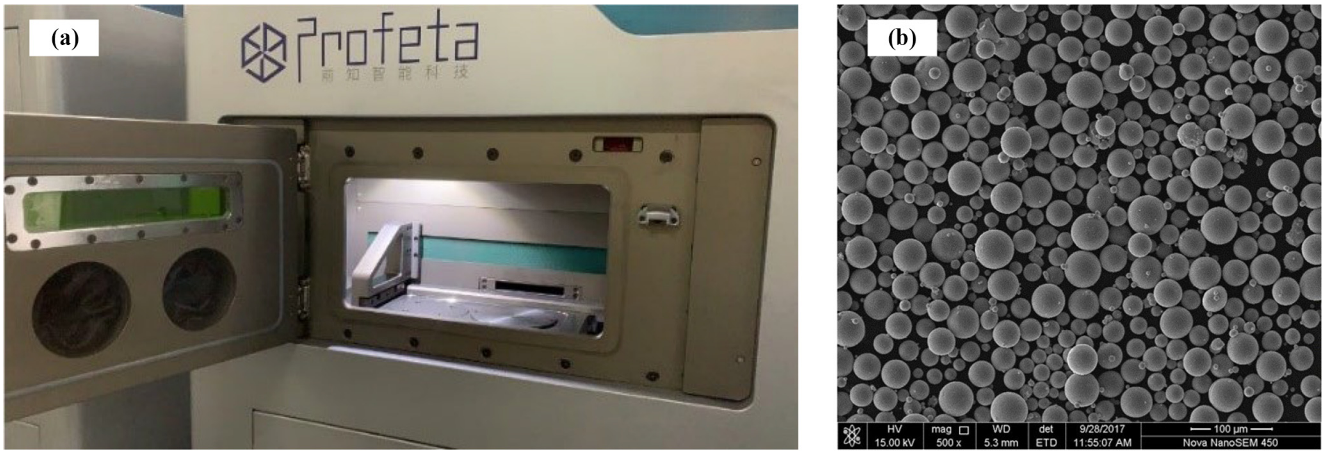

Figure 5 Main steps of capillary wick test piece 3D-printing manufacturing

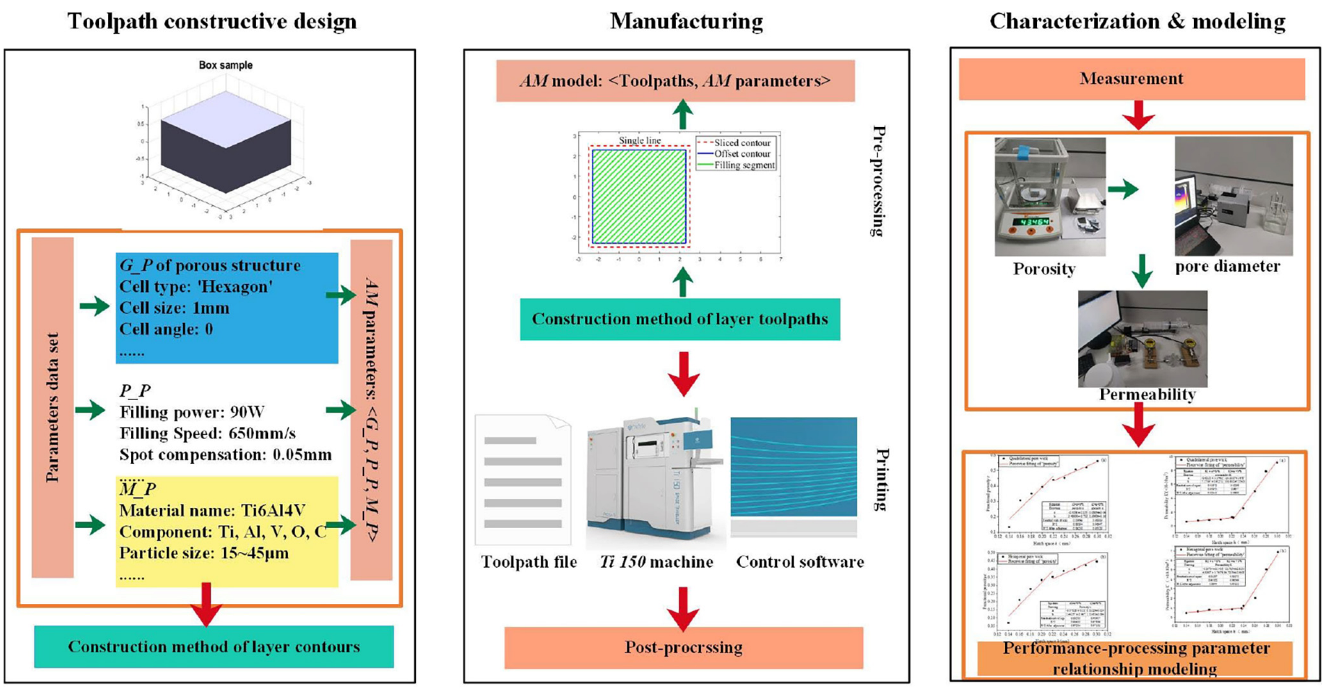

sample from the disk; sandblasting and airflow were used to clean residual particles from the channel; the final test pieces were obtained after ultrasonic cleaning for 30 min.

With the other parameters unchanged, nine quadrilateral pore wicks test piece and nine hexagonal pore wicks were designed by changing the hatch space. A total of 18 test pieces were manufactured.

As shown in Figure 6, two types of test pieces were produced by SLM printing. All test pieces were characterised using a measurement tool digital microscope system (RH-2000, Hirox, Japan) and a scanning electron microscope (Quanta 200 FEG). The OM images are shown in Figure 6(e) and (f). It is observed that quadrilateral and hexagonal pores of different diameters are formed in the capillary wicks test pieces with different hatching spaces.

3. Experimental device and experimental method

The capillary wick test piece performance test included three experiments: capillary wick test piece functional porosity measurement, pore diameter measurement and permeability measurement.

3.1 Functional porosity measurement

Functional porosity refers to the proportion of void volume in the capillary wick structure. Figure 7 shows a diagram of the

Rapid Prototyping Journal
Volume 28 · Number 8 · 2022 · 1558–1572

Table 1 Hatch space (*h*) during trajectory planning of two types of capillary wick test pieces

Quadrilateral pore hatch space *h* (mm)								
0.14	0.16	0.18	0.20	0.22	0.24	0.26	0.28	0.30
Hexagonal pore hatch space *h* (mm)								
0.14	0.16	0.18	0.20	0.22	0.24	0.26	0.28	0.30

Table 2 Constant parameters during the printing of the test piece

Print parameter	Value
Layer thickness (mm)	0.03
Spot compensation (mm)	0.05
Angle (°)/angle increment (°)	Quadrilateral pore: 45/90 Hexagon pore: 0/0
Start point	Random in the contour line
Contour number	1
Contour laser power (W)	75
Contour laser speed (mm/s)	2,800
Filling region offset distance (mm)	0

experimental device used to measure the functional porosity of the porous structure sample and the experimental site diagram.

The mass of the container and liquid mass (M_1) were measured before the test piece was immersed in the liquid. After one end of the test piece was immersed in the liquid and the liquid filled the internal voids of the capillary wick through capillary action, the total mass of the container and liquid (M_2) was measured. The total volume of the test piece (V) was calculated using the manufacturing dimensions of the test piece. The density of the liquid (ρ) was known; thus, the functional porosity of the porous structure (ε) was obtained using equation (1):

$$\varepsilon = \frac{M_1 - M_2}{\rho V} \times 100\% \tag{1}$$

3.2 Pore diameter measurement

A diagram of the experimental device for measurement of the capillary wick test pieces aperture is shown in Figure 8.

The effective pore diameter of the capillary wick was measured using the pressurised bubbling method (Luo *et al.*, 2019); air was injected into the closed cavity holding the test piece by the air pump and the lower end of the test piece was immersed in the liquid. The pressure was increased until bubbles appeared in the liquid and the gas pressure P in the closed cavity was measured using a pressure gauge. As the surface tension σ of the liquid was known, the effective capillary pore diameter R of the wick was obtained as:

$$R = \frac{2\sigma}{P} \tag{2}$$

During pressurisation, the air flow was evenly injected; the bubbling pressure P was measured when the first bubble appeared in the camera record. The surface tension of the liquid at room temperature (24°C) was obtained from a table (σ = 72.1 mN/m).

Figure 6 (a) 3D structure diagram of quadrilateral pore wick test piece; (b) SLM printed quadrilateral pore capillary wicks test piece (h = 0.30 mm); (c) OM picture of quadrilateral pore capillary wicks test piece (h = 0.30 mm); (d) 3D structure diagram of hexagonal pore wick test piece; (e) SLM printed hexagonal pore capillary wicks test piece (h = 0.30 mm); (f) OM picture of hexagonal pore capillary wicks test piece (h = 0.30 mm)

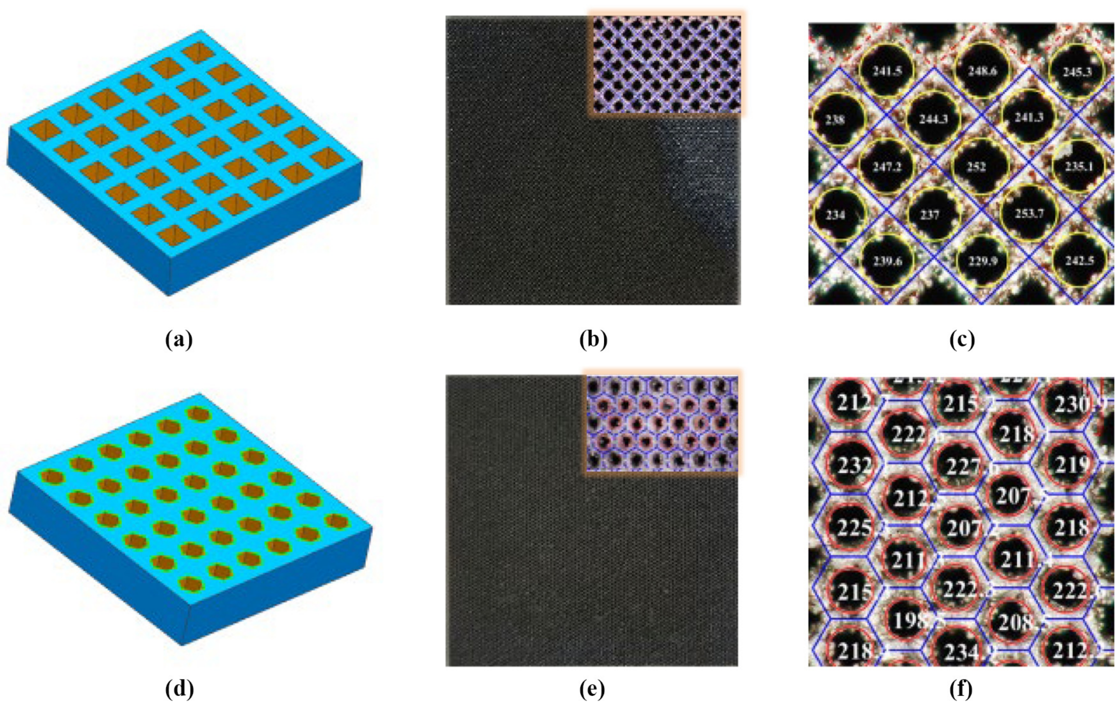

Figure 7 Schematic diagram and field diagram of functional porosity test experiment

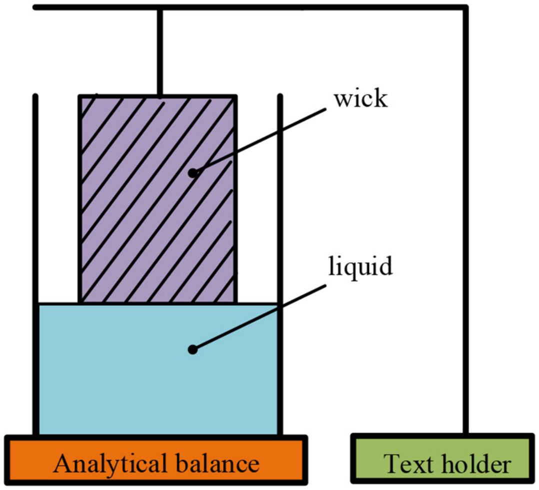

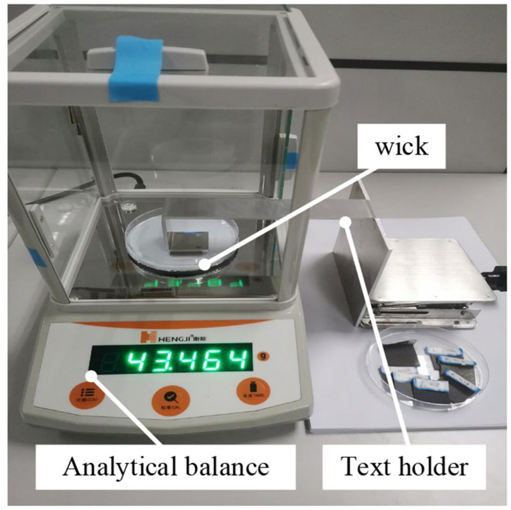

Figure 8 Schematic diagram and field diagram of pore diameter test experiment

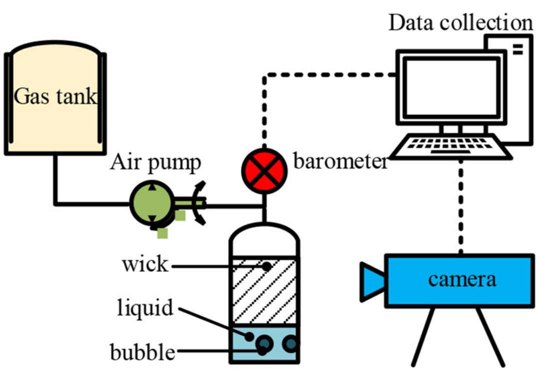

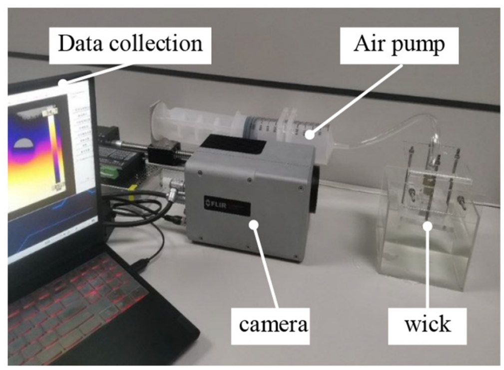

The microscopic pore diameter of the 3D-printed wick test piece was observed and measured using a scanning electron microscope to compare and analyse the experimental data.

3.3 Permeability measurement

The permeability of a porous medium is defined as the ability of the porous medium to allow liquid to pass through its internal pores (Hu *et al.*, 2020). Its value is related to the functional porosity, pore diameter and pore geometry in the direction of liquid penetration. With the complex pore structure, the permeability cannot be obtained directly; it can only be measured indirectly through experimental methods based on Darcy's law (Ma *et al.*, 2014). A diagram of the experimental device for measurement of the capillary wick permeability is shown in Figure 9.

The permeability can be obtained indirectly by measuring the pressure loss ΔP and the velocity of the liquid (v) flowing through the porous medium. The forced flow method is used to inject water at a constant speed into the flow cavity of the test area through a controllable-flow injection pump. With clamping the test piece, the pressure drop generated by flow channels outside the liquid working fluid was measured: $\Delta P_{\text{pipe}} = P_2' - P_1'$. The total pressure drop was measured by the pressure gauges at both ends of the test piece: $\Delta P_{all} = P_2 - P_1$. Thus, the pressure loss caused by the fluid flowing through the porous structure test piece is $\Delta P = \Delta P_{all} - P_{pipe}$; the permeability of the capillary wick test piece is expressed as:

$$\frac{\Delta P}{L} = \frac{\mu}{K}\nu \tag{3}$$

where L is the length of the test piece in the direction of fluid flow, μ is the viscosity of the liquid and v is the speed of liquid flow.

The liquid recovery device was connected to the end of the experimental device. The speed of fluid flow in the pipeline was controlled by adjusting the speed of the stepper motor and the size of the syringe. The liquid velocity on the pore scale must be in the Darcy state, which requires a Reynolds number $Re < 10$ (Dukhan *et al.*, 2014).

4. Experimental results and discussion

In this section, we experimentally explore the effects of pore diameter and pore shape on the permeability of porous

Figure 9 Permeability measurement experimental device: (a) schematic diagram and (b) physical diagram

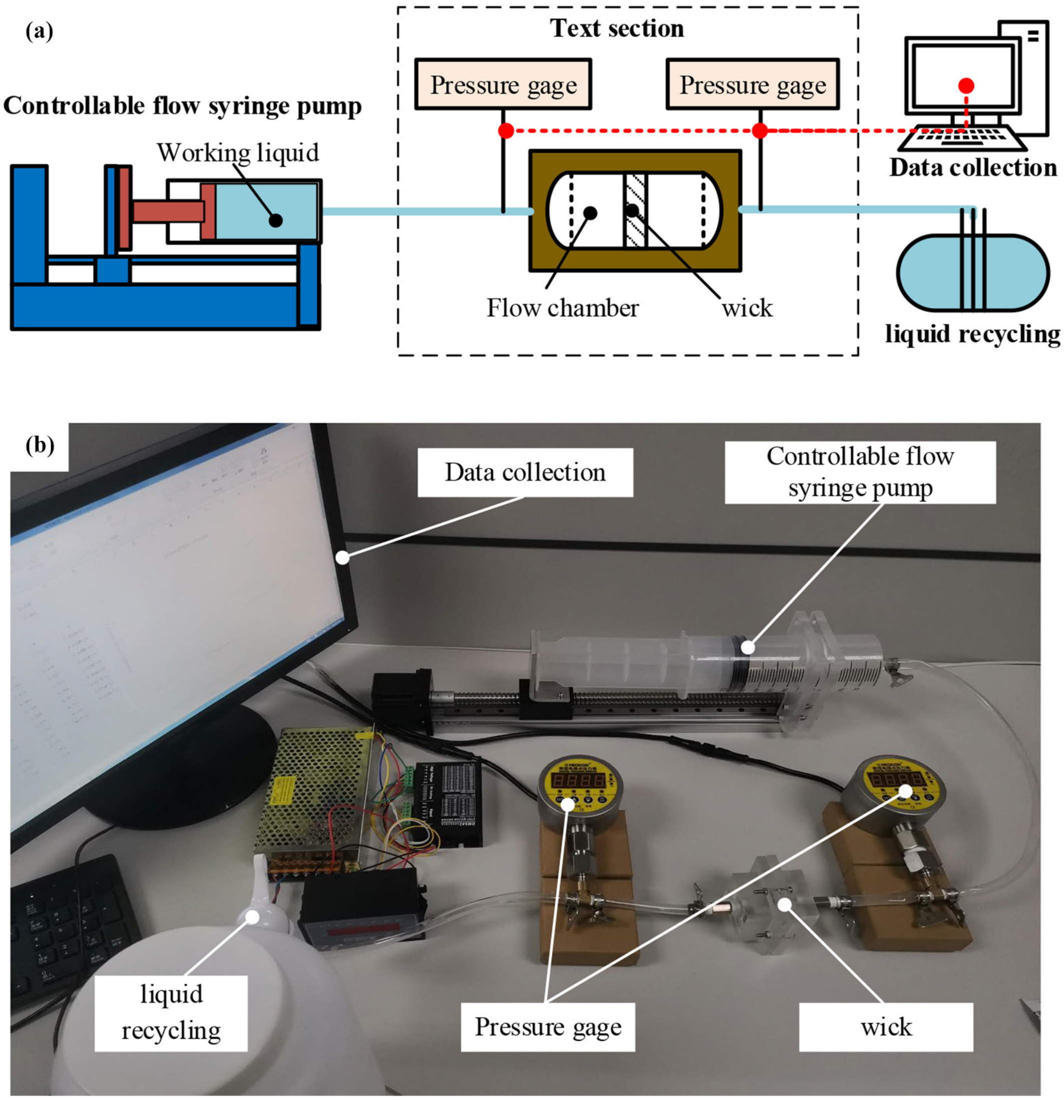

structures. The capillary wicks test pieces in the comparison analysis have the following three structures:

- traditional powder-sintered capillary wick test pieces;
- quadrilateral-pore SLM capillary wick test pieces; and
- hexagonal-pore SLM capillary wick test pieces.

The traditional manufacturing method for a powder-sintered capillary wick is the loose-powder sintering process (Weibel *et al.*, 2010). A metal powder with a diameter of 10–50 μm is filled inside the wick sleeve of the inserted inner wick rod. High-temperature sintering is conducted in a sintering furnace and the wick rod is removed to obtain the capillary wick. The performance parameters of the capillary wick were obtained from previous studies.

4.1 Pore diameter and functional porosity

The functional porosity corresponding to a traditional powder-sintered capillary wick with a certain effective pore diameter was obtained from previous studies, as shown in Table 3.

In this section, the pore diameters of two types of capillary wicks manufactured by SLM are obtained through a pressure foaming experiment and observations using scanning electron microscopy. The functional porosity of the capillary wick was measured using the Archimedes drainage method (Deng *et al.*, 2013). The measured pore diameters and porosities of the two types of capillary wicks are presented in Tables 4 and 5, respectively.

Figure 10(b) shows the change in the pore diameter with the hatch space for the two types of porous capillary wick test pieces. Overall, the pore diameters of the porous test pieces

Table 3 Traditional powder-sintered capillary wick pore diameter and functional porosity parameters (Ling *et al.*, 2018)

Pore diameter R (μm)	Functional porosity ε (%)
60	40.3
95	45.6
130	51.2

Table 4 Experimental data of pore diameter and functional porosity of SLM quadrilateral pore capillary wick test pieces

Hatch space h (mm)	Pore diameter R (μm)	Functional porosity ε (%)
0.14	78.00	13.54
0.16	92.75	30.62
0.18	103.05	35.23
0.20	119.30	39.45
0.22	138.20	43.92
0.24	168.38	45.37
0.26	193.50	50.69
0.28	225.03	52.02
0.30	253.17	56.26

Table 5 Experimental data of pore diameter and functional porosity of SLM hexagonal pore capillary wick test pieces

Hatch space h (mm)	Pore diameter R (μm)	Functional porosity ε (%)
0.14	73.00	6.92
0.16	88.00	21.23
0.18	96.13	27.85
0.20	105.30	33.29
0.22	108.26	35.31
0.24	130.17	38.94
0.26	165.07	40.13
0.28	195.75	42.44
0.30	215.50	44.70

increased with an increase in hatch space. In the early stage ($h <$ 0.22 mm), the pore diameter growth rate was slow; in the later stage ($h \geq$ 0.22 mm), the pore diameter growth rate was accelerated. Over the entire hatch space range, the pore diameter of the quadrilateral-pore capillary wick test pieces was larger than that of the hexagonal-pore capillary wick test pieces with the same hatch space. As shown in Figure 10(a), the functional porosity of the capillary wick test pieces manufactured by SLM increased with an increase in the hatch space, reaching a maximum when h = 0.30 mm: ε_q = 56.26%, ε_h = 44.70%.

When the hatch space is small ($h <$ 0.22 mm), the pore diameter and functional porosity of the SLM capillary wick test pieces are very small, possibly because of powder remelting and powder bonding during laser scanning, leading to fewer internal pores or the complete blockage of pores by powder. Figure 11 shows the phenomenon of powder bonding and pore blockage in the SLM capillary wick test piece when h = 0.16 mm. For the entire hatch space range, the pore diameter and functional porosity of the SLM quadrilateral-pore capillary wick test pieces were greater than those of the SLM hexagonal-pore capillary wick test pieces with the same hatch space. Actually, the porous structure filled with hexagon line achieves more energy than that filled with cross line. The reason is that the laser cannot switch start and stop immediately because these actions entail some delays. These delays will affect the energy received at the start and end points (called jump points), during the galvanometer marking the scanning path. At the

Figure 10 Comparative analysis (a) Functional porosity of porous structure changes with hatch space; and (b) pore diameter of porous structure changes with hatch space

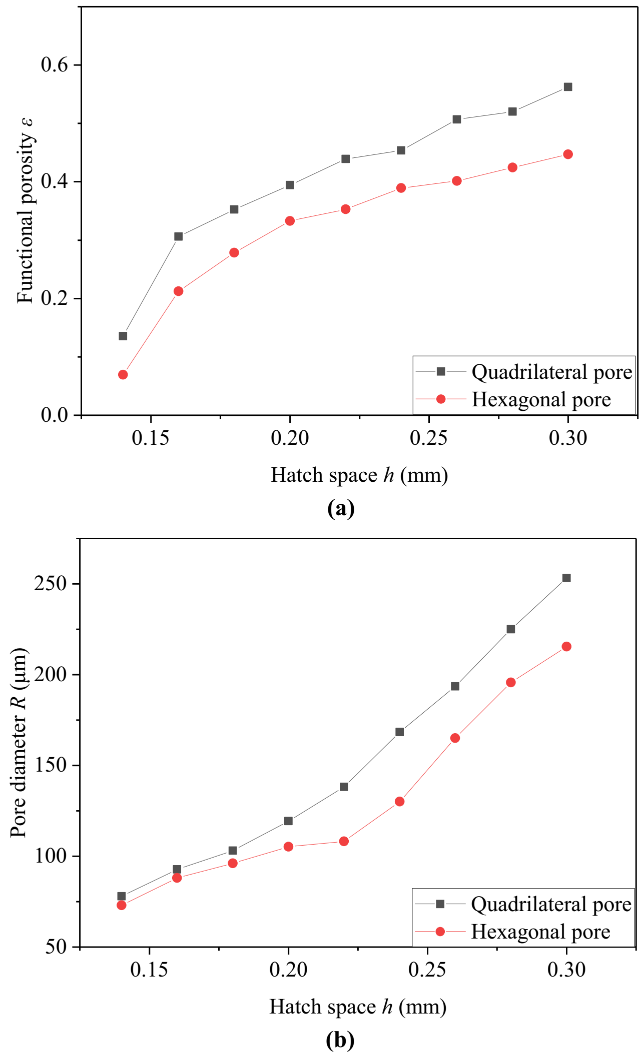

jump point, there will be a delay when the laser is turned off (Ding *et al.*, 2021). So, there is more energy input in the SLM fabrication of the hexagonal-pore capillary wick test piece, resulting in a decrease in inner pore diameter and functional porosity.

4.2 Permeability

4.2.1 Traditional powder sintered capillary wick

The permeability curves of traditional powder-sintered capillary wick test pieces with different pore diameters obtained from previous studies are shown in Figure 12.

In the permeability curve of a traditional powder-sintered capillary wick, the permeability increases with an increase in pore diameter. The permeability increases slowly with a pore diameter of 30–90 μm; the permeability increase accelerates with a pore diameter of $R >$ 90 μm. When the pore diameter was 130 μm, the permeability of the traditional powder-sintered capillary wick was 9.4×10^{-12} m^2.

Figure 11 (h = 0.16 mm). The powder bonding and the pore are blocked

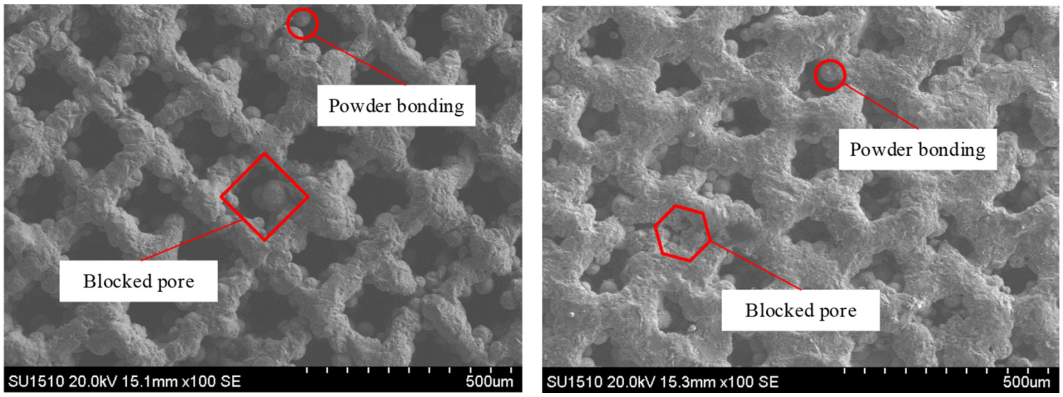

4.2.2 Selective laser melting capillary wicks

By adjusting the pulse input of the stepper motor, the flow rate of the liquid injected into the flow channel was controlled at 0.01 m/s, such that the liquid flow was in the Darcy flow state (Berti *et al.*, 2011).

Figure 13(a) shows that the permeability of the two types of SLM capillary wick test pieces increases with an increase in hatch space. When the hatch space is small (h < 0.22 mm), the permeability of the SLM capillary wick test pieces is low; the permeability increases rapidly with a hatch space of $h \geq$ 0.22 mm. The permeability of quadrilateral-pore SLM capillary wick test pieces is always greater than that of hexagonal-pore SLM capillary wick test pieces. As shown in Figure 13(b), the rising speed of the permeability curve is slow in the early stage and increases when the pore diameter is greater than 170 μm. With similar pore diameters, the two SLM capillary wick test pieces have a similar permeability.

Figure 12 Permeability of traditional powder-sintered capillary wick test pieces

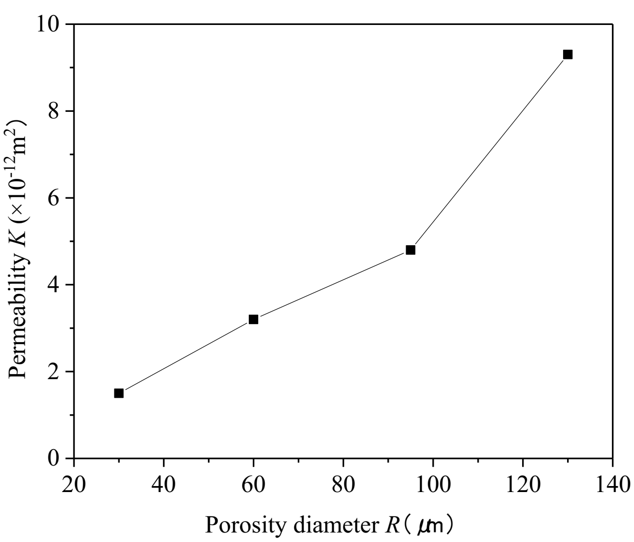

Figure 13 Comparative analysis (a) SLM capillary wick structure permeability changes with hatch space; and (b) SLM capillary wick structure permeability changes with pore diameter

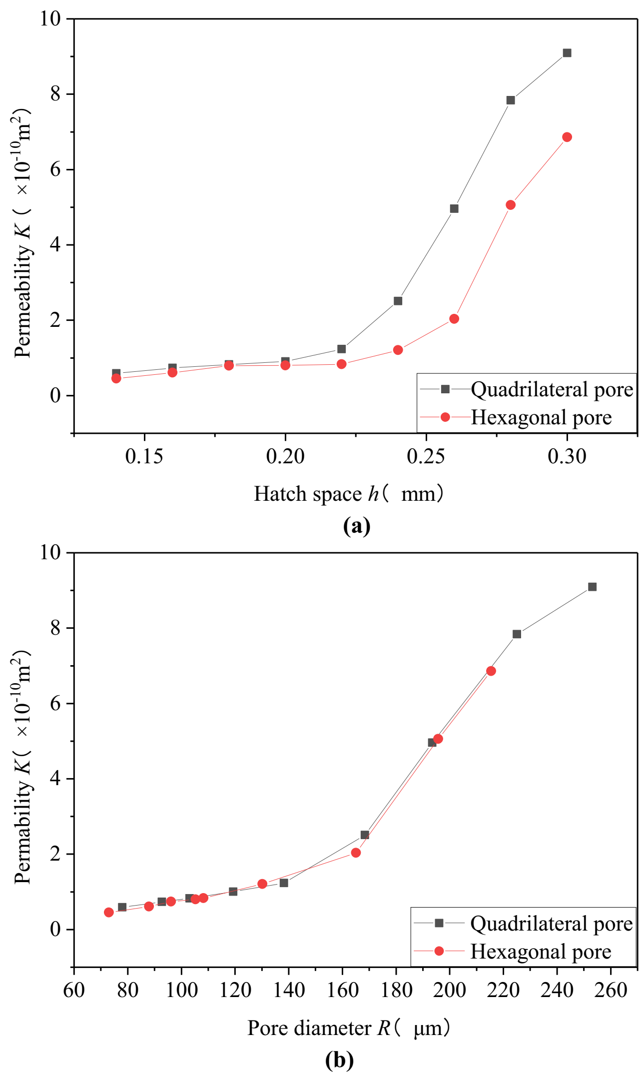

4.3 Selective laser melting versus traditional powder sintering

The functional porosity (ε) and permeability (K) of 3D-printed SLM capillary wick test pieces and traditional powder-sintered capillary wick test pieces with the same pore diameter were compared. The advantages and disadvantages of the 3D-printing SLM manufacturing process for heat pipe capillary wick structures were studied.

As shown in Figure 14, in the small pore size range, because of the small hatch space and serious powder binding, the functional porosity of 3D-printed SLM capillary wick is lower than that of traditional powder-sintered capillary wick. With the increasing pore size of 3D-printed SLM capillary wick, the powder bonding decreases and the functional porosity gradually increases. As shown in Figure 15, the permeability of the capillary wick test piece manufactured using traditional powder sintering was much lower than that of the capillary wick test piece manufactured by SLM. The histogram shows that when the pore diameter is approximately 130 μm, the permeability of the SLM capillary wick test piece is nearly 15 times that of a traditional powder-sintered capillary wick test piece.

The inner pores of a capillary wick test piece manufactured by traditional powder sintering are complex tortuous channels; many pores are blocked by powder because the sintering temperature is difficult to accurately control (Wu *et al.*, 2006). Unlike traditional powder-sintered capillary wick test pieces, the internal pores in the SLM capillary wick test piece are regular straight channels; the pore diameter can be controlled by controlling the printing parameters. The regular straight channels with little blockage reduce the resistance of liquid flow and increase the permeability of the capillary wick test piece. The SLM process can produce a heat pipe capillary wick structure with better permeability than traditional powder sintering.

Figure 14 Permeability of traditional powder sintering process and SLM process

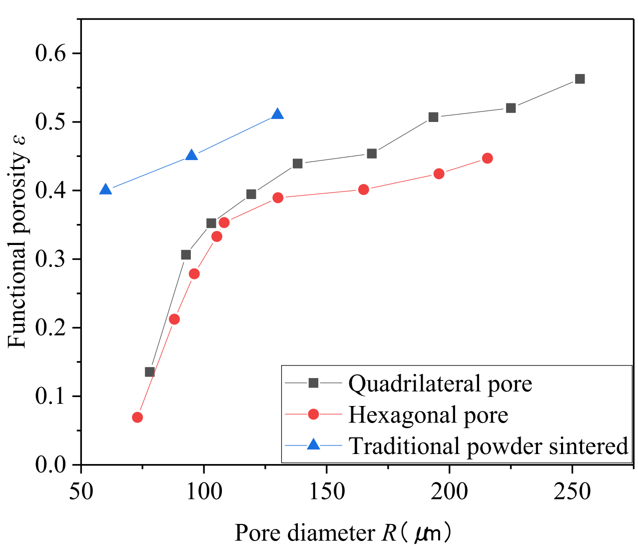

Figure 15 Permeability of capillary wicks at similar pore diameter

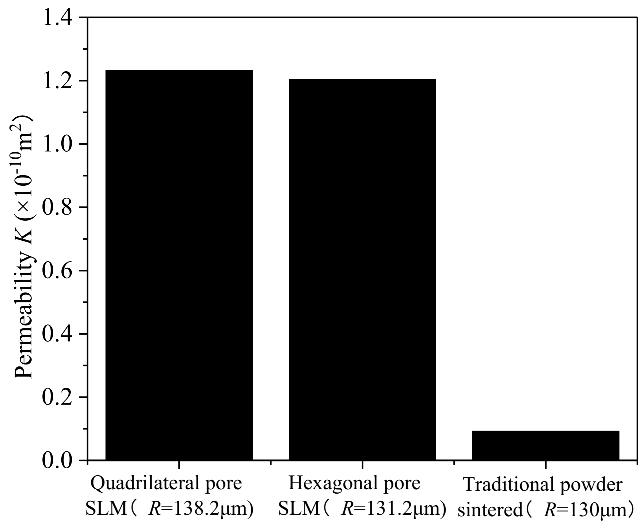

4.4 Performance-processing parameter relationship modeling

In this section, the functional porosity and permeability curves of SLM capillary wick test pieces with different hatch spaces are fitted using the collected experimental datasets. The relationships between the performance parameters of the SLM capillary wick test pieces and the hatch space are determined when other manufacturing parameters are fixed and may provide guidance for the design of SLM capillary wicks in the future.

4.4.1 Relationship between functional porosity and hatch space (ε–h)

The functional porosity curves were fitted using piecewise fitting; the fitting equation between the functional porosity of the SLM capillary wick test pieces and the hatch space was obtained when the other SLM parameters were fixed.

The fitting equation for functional porosity and hatch space of SLM capillary wick test pieces with quadrilateral pores is expressed as:

$$\varepsilon_q = f(h) = \begin{cases} -0.30 + 3.48 \times h, & 0.14 \ll h < 0.22 \\ 0.09 + 1.57 \times h, & 0.22 \ll h \ll 0.30 \end{cases} \tag{4}$$

The fitting equation for functional porosity and hatch space of SLM capillary wick test pieces with hexagonal pores is expressed as:

$$\varepsilon_h = f(h) = \begin{cases} -0.37 + 3.44 \times h, & 0.14 \ll h < 0.22 \\ 0.11 + 1.11 \times h, & 0.22 \ll h \ll 0.30 \end{cases} \tag{5}$$

According to Figure 16(a), the correlation coefficients for the two-part fitting models of the quadrilateral pore wicks were 0.882 and 0.966, respectively. Approximately 88.2% and

Figure 16 Data fitting results of SLM capillary wick test pieces functional porosity curves with respect to hatch space (a) quadrilateral pore and (b) hexagonal pore

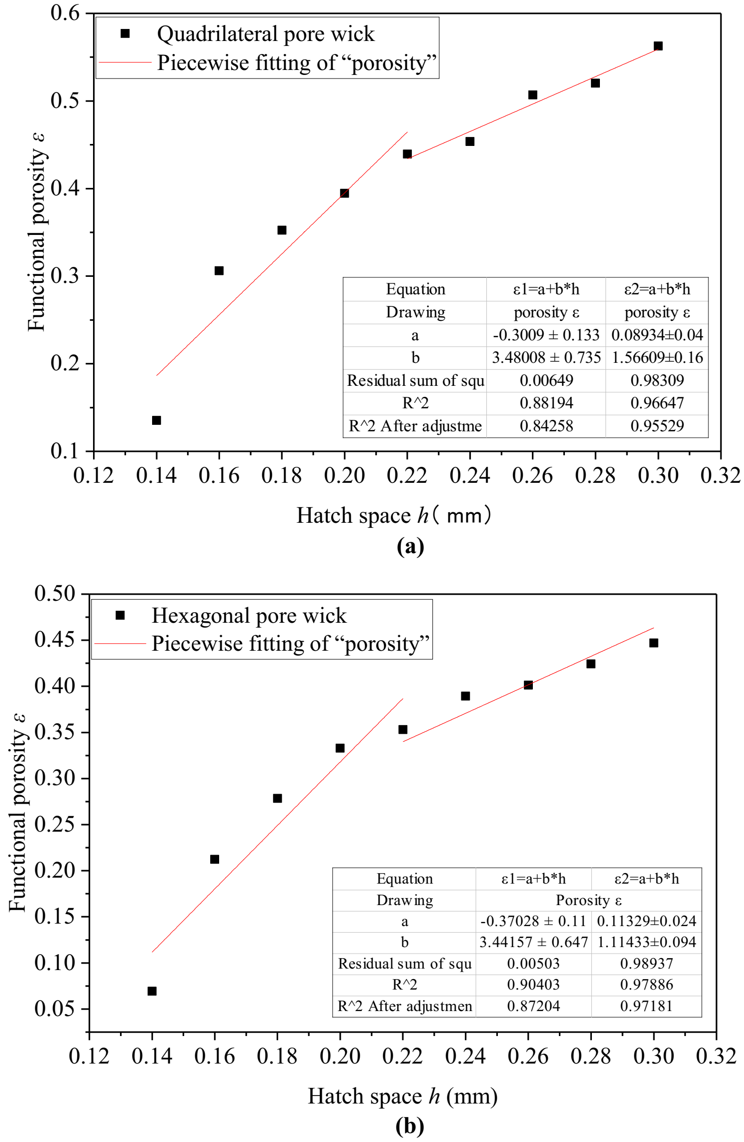

96.6% of the variance in the experimental data can be accounted for by the predicted output of equation (4). According to Figure 16(b), the correlation coefficients for the two-part fitting models of the hexagonal pore wicks were 0.904 and 0.978, respectively. Approximately 90.4% and 97.8% of the variance in the experimental data can be accounted for by the predicted output of equation (5).

4.4.2 Relationship between permeability and hatch space (K–h)

The permeability curves were fitted using piecewise fitting; the fitting equation between the permeability of the SLM capillary wicks and the hatch space was obtained when the other SLM parameters were fixed.

The fitting equation for permeability (K_q) and hatch space of SLM capillary wick test pieces with quadrilateral pores is expressed as:

$$K_q = f(h) = \begin{cases} (-0.45 + 7.25 \times h) \times 10^{-10}, & 0.14 \ll h < 0.22 \\ (-22.18 + 108.63 \times h) \times 10^{-10}, & 0.22 \ll h \ll 0.30 \end{cases} \tag{6}$$

The fitting equation for permeability (K_h) and hatch space of SLM capillary wick test pieces with hexagonal pores is expressed as:

$$K_h = f(h) = \begin{cases} (-0.17 + 4.81 \times h) \times 10^{-10}, & 0.14 \ll h < 0.22 \\ (-21.71 + 94.70 \times h) \times 10^{-10}, & 0.22 \ll h \ll 0.30 \end{cases} \tag{7}$$

According to Figure 17(a), the correlation coefficients for the two-part fitting models of the quadrilateral pore wick test

Figure 17 Data fitting results of SLM capillary wick test pieces permeability curves with respect to hatch space (a) Quadrilateral pore and (b) hexagonal pore

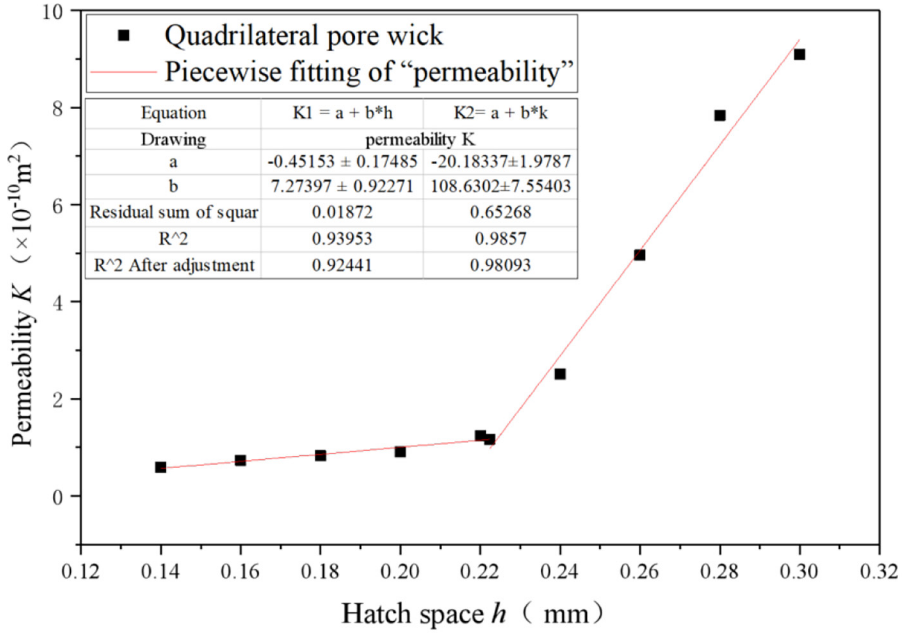

(a)

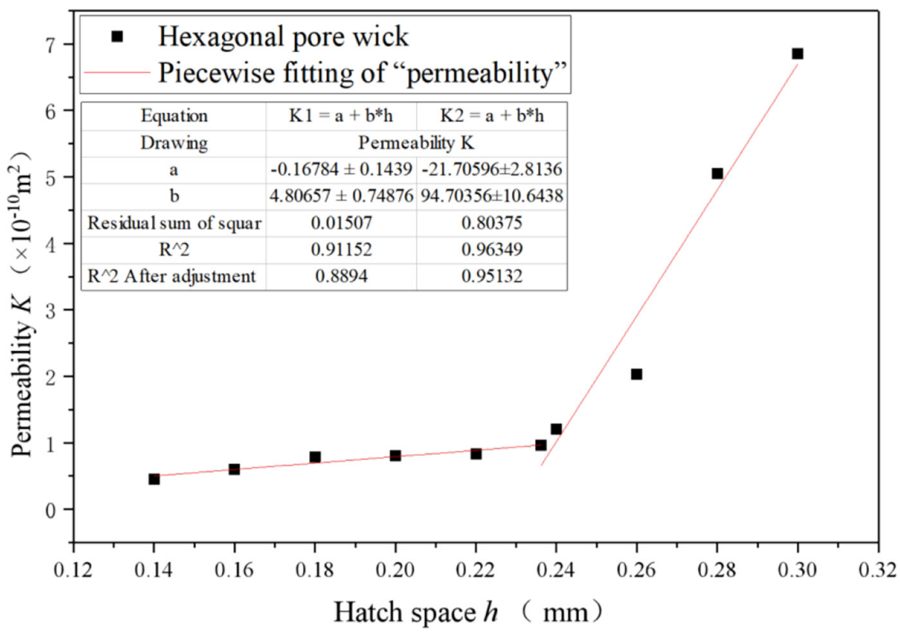

(b)

pieces were 0.939 and 0.986, respectively. Approximately 93.9% and 98.6% of the variance in the experimental data can be accounted for by the predicted output of equation (6). According to Figure 17(b), the correlation coefficients for the two-part fitting models of the hexagonal pore wick test pieces were 0.912 and 0.963, respectively. Approximately 91.2% and 96.3% of the variance in the experimental data can be accounted for by the predicted output of equation (7).

4.4.3 Summary and discussion

As the hatch space increases, the permeability changes linearly, but at two different rates. In the interval of 0.14 mm $\leq h \leq$ 0.22 mm, the permeability increases smoothly; in the interval of 0.22 mm $\leq h \leq$ 0.30 mm, the permeability increases rapidly. Different hatch spaces cause different quantities of powder to be adsorbed. As shown in Figure 18, when the hatch space is too small, re-melting occurs during the laser sintering process.

Figure 18 SEM picture of SLM capillary wick test pieces (a) quadrilateral pore and (b) hexagonal pore

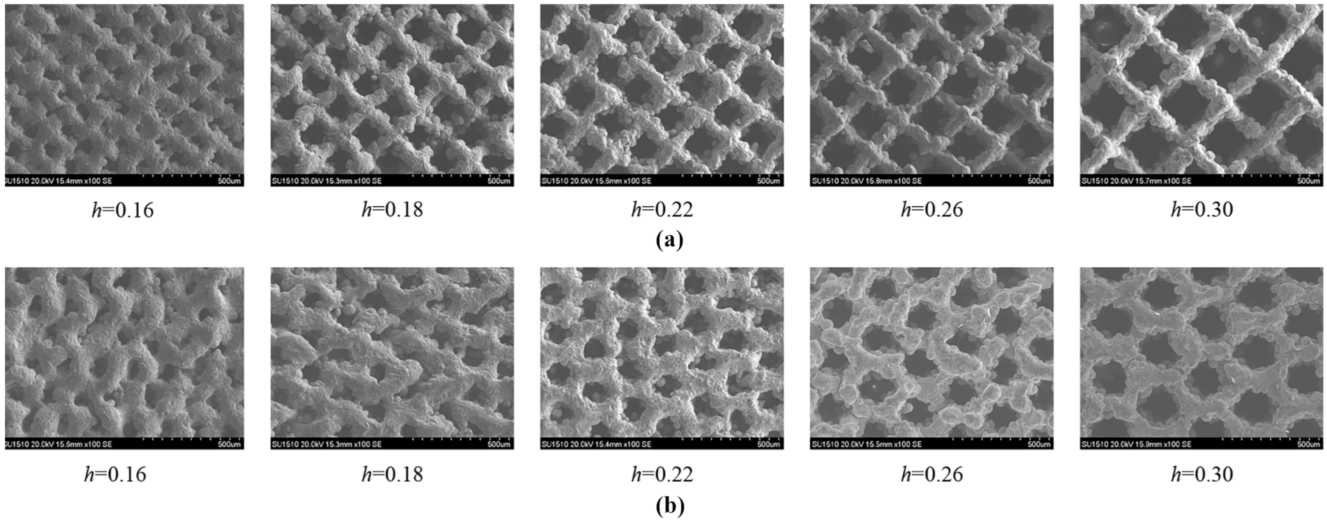

The metal powder attaches to the melt channels in a molten/semi-melted state, causing the internal channels of the printed capillary wick test piece to shrink or be completely blocked by the non-fused raw powders, which are usually difficult to remove in the post-processing stage. When the distance between laser sintering paths is increased into the range of $0.22\,\text{mm} \leq h \leq 0.30\,\text{mm}$, the extent of re-melting and the resulting powder adsorption are reduced and more unobstructed channels are generated. The porous structure has a greater functional porosity and permeability because the non-fused raw material powders can be easily removed during the post-processing stage. The functional porosity and permeability of the SLM capillary test pieces follow different change rates with hatch spaces greater than and less than 0.22 mm.

With the calculated correlation coefficient, the curve equation obtained by polynomial fitting can represent the functional relationship between the functional porosity, permeability and the hatch space in printing and provide a reference for capillary wick design and printing in industrial applications.

5. Conclusion

An experimental manufacturability investigation demonstrated that the SLM process can be used to print fine porous structures with a pore size of 100 μm with stable processing control. The SLM process can print a series of porous structures with different pore diameters by changing the hatch space. A larger SLM hatch space produces a better printed porous structure. It is possible to print porous capillary wick structures with holes of different shapes by controlling the laser scanning path. The shape of the pores affects the SLM printing of the capillary wick porous structure; a more complex pore generation path produces a smaller pore size, functional porosity and permeability with the same hatch space. The comparative analysis showed that the permeability of the 3D-printed capillary wick structure was much greater than that of a traditional powder-sintered capillary wick structure with the same pore size. When R = 130 μm, the permeability was 15 times greater than that of a traditional powder-sintered capillary wick structure. These data indicate that SLM 3D-printing manufacturing technology has great potential for capillary wick manufacturing. The functional porosity and permeability of quadrilateral and hexagonal porous structures printed by SLM reflect a certain functional relationship with the hatch space. The fitting equations for the functional porosity and permeability of SLM capillary wick test pieces with two pore shapes with respect to the hatch space were obtained using piecewise fitting and can provide a data reference for capillary wick design with 3D printing.

In future research, we will improve the design of the capillary wick structure and the post-processing method and use the SLM process for the manufacture of complete heat pipes.

References

Berti, L., Santos, P., Bazzo, E., Janssen, R., Hotza, D. and Rambo, C. (2011), "Evaluation of permeability of ceramic wick structures for two phase heat transfer devices", *Applied Thermal Engineering*, Vol. 31 Nos 6/7, pp. 1076-1081.

Bonnici, M., Mollicone, P., Fenech, M. and Azzopardi, M.A. (2019), "Analytical and numerical models for thermal related design of a new Pico-satellite", *Applied Thermal Engineering*, Vol. 159, p. 113908.

Deng, D., Liang, D., Tang, Y., Peng, J., Han, X. and Pan, M. (2013), "Evaluation of capillary performance of sintered porous wicks for loop heat pipe", *Experimental Thermal and Fluid Science*, Vol. 50, pp. 1-9.

Ding, L., Tan, S., Chen, W., Jin, Y. and Zhang, Y. (2021), "Manufacturability analysis of extremely fine porous structures for selective laser melting process of Ti6Al4V alloy", *Rapid Prototyping Journal*, Vol. 27 No. 8, pp. 1523-1537.

Dukhan, N., Bağcı, Ö. and Özdemir, M. (2014), "Metal foam hydrodynamics: flow regimes from pre-Darcy to turbulent", *International Journal of Heat and Mass Transfer*, Vol. 77, pp. 114-123.

Esarte, J., Blanco, J.M., Bernardini, A. and Sancibrián, R. (2019), "Performance assessment of a three-dimensional printed porous media produced by selective laser melting technology for the optimization of loop heat pipe wicks", *Applied Sciences*, Vol. 9 No. 14, p. 2905.

Escobar, E., Diaz, M. and Zagal, J.C. (2016), "Evolutionary design of a satellite thermal control system: real experiments for a cube sat mission", *Applied Thermal Engineering*, Vol. 105, pp. 490-500.

Faghri, A. (1995), *Heat Pipe Science and Technology*, Global Digital Press, United States.

Faghri, A. (2012), "Review and advances in heat pipe science and technology", *Journal of Heat Transfer*, Vol. 134 No. 12, pp. 148-166.

Hu, Z., Wang, D., Xu, J. and Zhang, L. (2020), "Development of a loop heat pipe with the 3D printed stainless steel wick in the application of thermal management", *International Journal of Heat and Mass Transfer*, Vol. 161, p. 120258.

Hu, J., Qian, Z., Liu, P., Wang, D. and Oeser, M. (2020), "Investigation on the permeability of porous asphalt concrete based on microstructure analysis", *International Journal of Pavement Engineering*, Vol. 21 No. 13, pp. 1683-1693.

Jafari, D., Wits, W.W. and Geurts, B.J. (2017), "An investigation of porous structure characteristics of heat pipes made by additive manufacturing", *2017 23rd International Workshop on Thermal Investigations of ICs and Systems (THERMINIC)*, IEEE, pp. 1-7.

Jafari, D., Wits, W.W. and Geurts, B.J. (2018), "Metal 3D-printed wick structures for heat pipe application: capillary performance analysis", *Applied Thermal Engineering*, Vol. 143, pp. 403-414.

Lebaal, N., Zhang, Y., Demoly, F., Roth, S., Gomes, S. and Bernard, A. (2019), "Optimised lattice structure configuration for additive manufacturing", *CIRP Annals*, Vol. 68 No. 1, pp. 117-120.

Ling, W., Zhou, W., Yu, W. and Chu, X. (2018), "Capillary pumping performance of porous copper fiber sintered wicks for loop heat pipes", *Applied Thermal Engineering*, Vol. 129, pp. 1582-1594.

Lu, X., Thomas, P.J., Zhang, Y., Liao, H., Gomes, S. and Hellevang, J.O. (2020), "Characterization of optical fibers directly embedded on metal using a particle Spray-Based method", *IEEE Sensors Journal*, Vol. 20 No. 12, pp. 6414-6421.

Luo, S., Wang, Q., Ye, R. and Ramachandran, C.S. (2019), "Effects of electrolyte concentration on the microstructure and properties of plasma electrolytic oxidation coatings on Ti-6Al-4V alloy", *Surface and Coatings Technology*, Vol. 375, pp. 864-876.

Ma, D., Miao, X., Jiang, G., Bai, H. and Chen, Z. (2014), "An experimental investigation of permeability measurement of water flow in crushed rocks", *Transport in Porous Media*, Vol. 105 No. 3, pp. 571-595.

Shittu, S., Li, G., Zhao, X., Zhou, J., Ma, X. and Akhlaghi, Y. G. (2020), "Experimental study and exergy analysis of photovoltaic-thermoelectric with flat plate micro-channel heat pipe", *Energy Conversion and Management*, Vol. 207, p. 112515.

Sözen, A., Gürü, M., Khanlari, A. and Çiftçi, E. (2019), "Experimental and numerical study on enhancement of heat transfer characteristics of a heat pipe utilizing aqueous clinoptilolite nanofluid", *Applied Thermal Engineering*, Vol. 160, p. 114001.

Vaneker, T., Bernard, A., Moroni, G., Gibson, I. and Zhang, Y. (2020), "Design for additive manufacturing: framework and methodology", *CIRP Annals*, Vol. 69 No. 2, pp. 578-599.

Weibel, J.A., Garimella, S.V. and North, M.T. (2010), "Characterization of evaporation and boiling from sintered powder wicks fed by capillary action", *International Journal of Heat and Mass Transfer*, Vol. 53 Nos 19/20, pp. 4204-4215.

Wong, S.C. and Liao, W.-S. (2018), "Visualization experiments on flat-plate heat pipes with composite mesh-groove wick at different tilt angles", *International Journal of Heat and Mass Transfer*, Vol. 123, pp. 839-847.

Wu, J.Y. Hong, C.W. Lo, C.T. and Cheng, C.T. (2006), "Heat pipe with sintered powder wick", in, Google Patents.

Yan, B.H., Wang, C. and Li, L.G. (2020), "The technology of micro heat pipe cooled reactor: a review", *Annals of Nuclear Energy*, Vol. 135, p. 106948.

Zhang, Y., Tan, S., Ding, L. and Bernard, A. (2021), "A tool-path construction design method for fine porous structure design & printing in additive manufacturing", *CIRP Annals - Annals*, Vol. 70 No. 1, pp. 123-126, doi: 10.1016/j.cirp.2021.04.020.

Zhang, Y., Wang, Z., Zhang, Y., Gomes, S. and Bernard, A. (2020), "Bio-inspired generative design for support structure generation and optimization in additive manufacturing (AM)", *CIRP Annals*, Vol. 69 No. 1, pp. 117-120.

Corresponding authors

Liheng Chen can be contacted at: chenliheng3@163.com, and **Yicha Zhang** can be contacted at: yicha.zhang@utbm.fr